Synergistic metal-ligand redox-cooperativity for electrocatalytic CO_2 reduction promoted by a ligand-based redox couple in Mn and Re tricarbonyl complexes

Meaghan McKinnon[†], Ken T. Ngo[†], Sebastian Sobottka[‡], Biprajit Sarkar[‡], Mehmed Z. Ertem[¥]*, David C. Grills[¥]* and Jonathan Rochford[†]*

†Department of Chemistry, University of Massachusetts Boston, 100 Morrissey Boulevard, Boston, MA 02125, USA. ‡Institut für Chemie und Biochemie, Anorganische Chemie, Freie Universität Berlin, Fabeckstrasse 34-36, Berlin, Germany. [¥]Chemistry Division, Brookhaven National Laboratory, Upton, NY, 11973-5000, USA.

Supporting Information Placeholder

ABSTRACT: Electrocatalytic CO_2 reduction is demonstrated for the Mn and Re tricarbonyl complexes, $[M(Me_2OQN)(CO)_3(CH_3CN)]$ (M = Mn or Re) containing the 5,7-dimethyl-8-oxyquinolate (Me_2OQN^-) ligand. In comparison to the related 2,2'-bipyridyl (bpy) reference complexes, $[M(bpy)(CO)_3(CH_3CN)]^+$ (M = Mn or Re), the Me_2OQN^--based pre-catalysts exhibit onset of catalytic current with the input of one less equivalent of electrons. This behavior is attributed to the formal $Me_2OQN^{(\bullet/-)}$ redox couple which contributes towards each catalytic cycle in tandem with the formal $Mn^{I/0}$ and $Re^{I/0}$ redox couples. In addition to computational support for synergistic metal-ligand redox-cooperativity, electrochemistry (cyclic voltammetry and controlled potential electrolysis), spectroelectrochemistry (FTIR and EPR), and pulse radiolysis coupled with time-resolved infrared (TRIR) spectroscopy, provide structural insight into the electronic properties of the one-electron and two-electron reduced species.

INTRODUCTION

The harvesting and storage of solar energy in the form of chemical bonds via electrocatalytic CO_2 conversion with solar-derived electricity is highly desired. Of the many classes of homogeneous transition metal catalysts investigated for CO_2 reduction, the $[Mn(\alpha\text{-diimine})(CO)_3L]^n$ systems, where L is a neutral or anionic monodentate ligand such as acetonitrile (CH_3CN; n = 1+) or Br^- (n = 0), are among the most highly studied.[1, 2] This is in part due to the abundance and low-cost of manganese but also due to the capacity for these catalysts to exhibit a high turnover frequency (TOF),[3, 4] and a tunable and high product selectivity with, on occasion, a high turnover number (TON).[5, 6] The majority of these studies have utilized conventional 2,2'-bipyridyl (bpy)-based α-diimine ligands, inspired no doubt by the early works of Hawecker, Lehn and Ziessel[7, 8], and Meyer[9] on $[ReCl(bpy)(CO)_3]$, as well as the more recent study by Chardon-Noblat, Deronzier and co-workers on $[MnBr(dmbpy)(CO)_3]$ (dmbpy = 4,4'-dimethyl-2,2'-bipyridine).[10] In contrast to their Re(I) analogues, apart from select examples,[4, 11-13] Mn(I)-based pre-catalysts typically require the presence of excess Brønsted acid for the binding of CO_2 and formation of a key Mn(I) metallocarboxylic acid intermediate.[14, 15] An increasing number of these Mn-based catalysts now deviate from the traditional α-diimine ligand framework, taking advantage of a variety of symmetric and asymmetric ligand scaffolds.[1] For example, Agarwal and co-workers first employed this approach through the introduction of the asymmetric 2-pyridyl *N*-heterocyclic carbene (NHC) ligand in a manganese(I) tricarbonyl bromide pre-catalyst, later improved upon with the more π-acidic 2-pyrimidyl NHC ligand.[16, 17] This work was followed by Hartl, Weinstein, and co-workers who developed a series of catalysts based upon the asymmetric 2-(phenylimino)pyridine ligand system where imine substituents were used to tune the redox properties of the Mn(I) center while 2,6-phenyl substituents were used to introduce steric bulk.[18] More recently, Richeson and co-workers reported highly selective CO evolution by the $[mer\text{-}Mn(PNP)(CO)_3]^+$ and $[fac\text{-}MnBr(PN)(CO)_3]$ pre-catalysts, where PNP is the *N*,*N*'-bis(diphenylphosphino)-2,6-di(methylamino)pyridine pincer ligand and PN is the bidentate *N*-(diphenylphosphino)-2-(methylamino)pyridine ligand.[12] Adopting a symmetric approach, Royo, Lloret-Fillol, and co-workers used a methylene bridged bidentate bis(*N*-methylimidazolium) ligand which exhibited the highest TOF_{max} for any Mn-based electrocatalyst reported to date, albeit with an inherently high overpotential due to the electron-rich properties of the ligand.[4]

In this study, the asymmetric bidentate electron-rich 5,7-dimethyl-8-oxyquinolate (Me_2OQN^-) ligand is investigated at both Re(I) and Mn(I) *facial*-tricarbonyl solvated metal centers, and compared against the redox and electrocatalytic properties of their Re(I) and Mn(I) bpy counterparts for reference (Fig. 1).

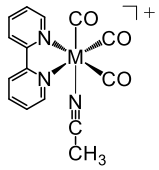

[1-Re-MeCN]$^{+}$ M = Re(I)
[1-Mn-MeCN]$^{+}$ M = Mn(I)

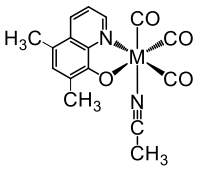

[2-Re-MeCN] M = Re(I)
[2-Mn-MeCN] M = Mn(I)

Figure 1. Molecular structures of $[M(bpy)(CO)_3(CH_3CN)]^+$ (**[1-M-MeCN]**$^+$, M = Re(I) or Mn(I)) and $[M(Me_2OQN)(CO)_3(CH_3CN)]$ (**[2-M-MeCN]**, M = Re(I) or Mn(I)).

This design is inspired by the copper-based monoamine and galactose oxidase enzymes, where a tyrosine O-radical/anion redox couple works in synergy with the Cu(II/I) redox couple to promote two-electron two-proton coupled amine/alcohol oxidation and dioxygen reduction.[19-22] Indeed, metalloradicals and redox transformations are the cornerstone of most catalytic cycles with growing importance today being given to catalysts possessing so-called '*non-innocent*' ligands[23, 24] which may be directly involved in the redox transformations of the catalytic cycle.[25-30] In this study, using a suite of experimental and computational techniques, we test the hypothesis that a ligand-based radical/anion redox couple may participate synergistically with the Re(I/0) or Mn(I/0) couple to effect the two-electron two-proton coupled reduction of CO_2 to CO. This demonstrates that both ligand and metal can share redox accountability, contributing one electron each towards catalyst activation, and ultimately CO evolution.

RESULTS

Synthesis and Structural Characterization

The syntheses of **[1-Re-MeCN]**$^+$, **[1-Mn-MeCN]**$^+$, and **[2-Re-MeCN]** were successfully completed following previously reported literature procedures.[31-33] Unlike in the previous report for **[2-Re-MeCN]**,[32] **[2-Mn-MeCN]** could not be isolated directly. Instead, the $[Mn(Me_2OQN)(CO)_3(THF)]$ complex was firstly prepared by deprotonating the commercially available 5,7-dimethyl-8-hydroxyquinoline ligand with a slight excess of potassium carbonate in dry tetrahydrofuran, followed by addition of bromopentacarbonyl manganese(I) and heating in a microwave reactor at 60 °C for 1 hour. Cooling to room temperature and recrystallization yielded analytically pure product. The $[Mn(Me_2OQN)(CO)_3(THF)]$ complex exhibits very similar solvation behavior to **[2-Re-MeCN]**, whereby in non-coordinating solvents the weakly bound monodentate THF ligand dissociates, forming the $[Mn(Me_2OQN)(CO)_3]_2$ dimer as confirmed by FTIR spectroscopy in dichloromethane. Similar again to **[2-Re-MeCN]**, immediate solvation of the dimer occurs in neat acetonitrile, quantitatively forming **[2-Mn-MeCN]** in-situ (Scheme 1), confirmed by FTIR (Fig. 2) and ^{1}H NMR (Fig. SI-1) spectroscopy.

Scheme 1. Solvation of the $[M(Me_2OQN)(CO)_3]_2$ dimer in acetonitrile, forming the acetonitrile solvated [2-M-MeCN] monomers (M = Mn or Re)

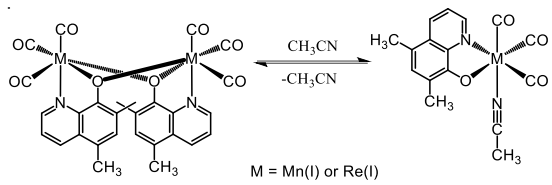

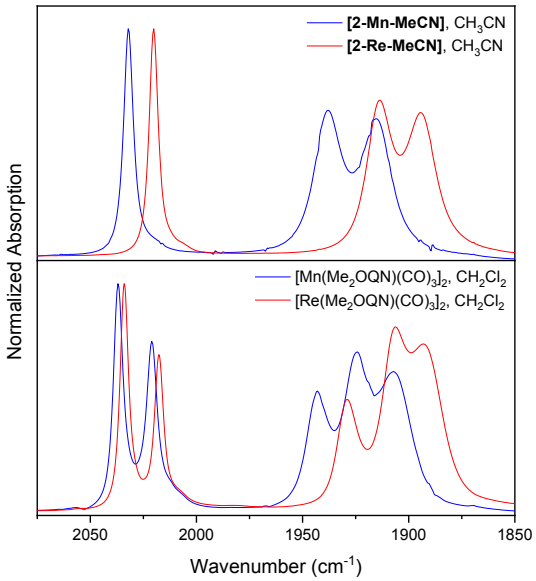

Figure 2. Overlay of FTIR spectra for **[2-Re-MeCN]** and **[2-Mn-MeCN]** recorded in acetonitrile (top), and the dimeric $[M(Me_2OQN)(CO)_3]_2$ (M = Mn or Re) complexes recorded in dichloromethane (bottom).

The FTIR spectra of both monomer and dimer Mn or Re complexes exhibit characteristic ν(CO) stretching modes in the 1850−2050 cm^{-1} range. In non-coordinating dichloromethane, the $[M(Me_2OQN)(CO)_3]_2$ (M = Mn or Re) spectra are best described as symmetric and asymmetric combinations of both *fac*-$M(CO)_3$ centers in the dimeric structure. The Mn dimer exhibits a symmetric and asymmetric combination of each tricarbonyl A(1)′ stretching mode at 2037 and 2021 cm^{-1}, while the equivalent Re dimer bands are shifted to slightly lower wavenumber, at 2034 and 2017 cm^{-1}, consistent with the Re center being more electron rich. The three absorption bands observed for the $[Mn(Me_2OQN)(CO)_3]_2$ dimer in dichloromethane at 1943, 1924 and 1907 cm^{-1} are due to unresolved overlap of four ν(CO) stretches due to symmetric and asymmetric coupling of each $Mn(CO)_3$ center A(2)′ and A″ stretching modes. Again, the Re dimer exhibits a similar profile but shifted to lower wavenumbers at 1929, 1906 and 1893 cm^{-1}. In acetonitrile, both the **[2-Mn-MeCN]** and **[2-Re-MeCN]** monomers exhibit the more common three peak profile typically observed for *fac*-tricarbonyl metal complexes possessing pseudo-C_s point group symmetry. **[2-Mn-MeCN]** exhibits A(1)′, A(2)′, and A″ ν(CO) stretching modes at 2032, 1938 and 1915 cm^{-1}, respectively.

The analogous ν(CO) stretching modes for the more electron rich Re complex, **[2-Re-MeCN]**, are observed at lower energy due to greater Re $d(\pi)\rightarrow$CO(π^*) back-donation, with peaks at 2020, 1913 and 1894 cm^{-1}.

Electronic structure calculations and cyclic voltammetry under 1 atm of argon

Prior to electrocatalysis studies it is important to gain an in-depth understanding of pre-catalyst redox properties under inert conditions in the absence of CO_2. In this particular study it is also relevant to highlight the unique redox characteristics of Re and Mn tricarbonyl complexes with the non-innocent Me_2OQN^- ligand. In a previous study by Zhao et al.,[32] the 'redox-active' label for the bpy ligand was distinguished from the more complex 'non-innocent ligand'[34] character of the Me_2OQN^- ligand in **[2-Re-MeCN]**, at least at its HOMO, HOMO-2 and HOMO-3 energy levels. Computational analysis predicts the HOMO level of **[1-Re-MeCN]**$^+$ to consist primarily of Re(d) and CO(π^*) character, with no contribution from the bpy ligand, whereas the non-innocent nature of the Me_2OQN^- ligand arises from degenerate mixing of the frontier Re $d(\pi)$ and Me_2OQN^- π-electron donating orbitals at the HOMO and HOMO-2 levels.[32] In the current study, to aid with electrochemical redox assignments, we investigated the net unpaired spin densities of the oxidized and reduced forms of **[2-Re-MeCN]** and **[2-Mn-MeCN]** as presented in Figure 3.

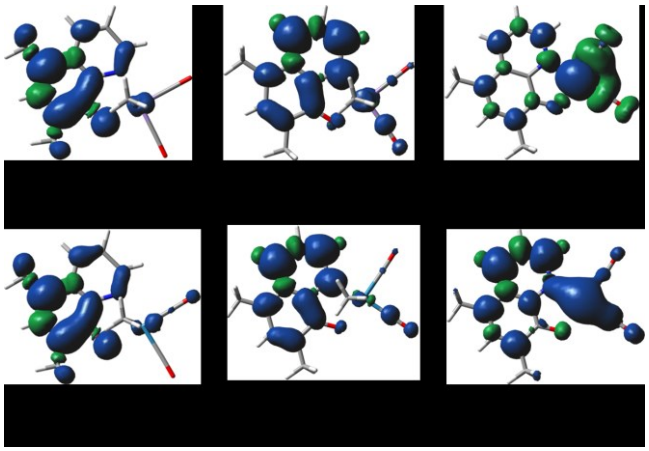

Figure 3. Spin density plots (isofactor = 0.001) computed at the M06 level of theory illustrating the significant contribution of the Me_2OQN^- ligand to the one-electron oxidized **[2-M-MeCN]**$^+$ complex, and the one-electron reduced six-coordinate **[2-M-MeCN]**$^-$ and five-coordinate **[2-M]**$^-$ complexes (M = Mn or Re).

One-electron oxidation of both **[2-Re-MeCN]** and **[2-Mn-MeCN]** leads to negligible net spin densities on the metal centers whereas significant spin is found to be delocalized on the phenolate ring of Me_2OQN^-, with ρ_O = 0.22-0.24. As a result, the oxidized species could be assigned as [M^I-($Me_2OQN^{\bullet}$)(MeCN)]$^+$. Similarly, one-electron reduction results in the reduction of the ligand, which could be viewed as [M^I($Me_2OQN^{\bullet-}$)(MeCN)]$^-$. However, this time higher spin density is localized on the pyridyl-side of the quinioline ring with ρ_N = 0.23 and ρ_O = 0.01, indicating negligible radical character on the oxygen atom. Upon dissociation of the acetonitrile ligand, the unpaired spin localizes on the metal center for **[2-Mn]**$^-$ (ρ_{Mn} = 1.36) whereas it is shared between the Me_2OQN ligand and the metal center for **[2-Re]**$^-$ (ρ_{Re} = 0.22) (Fig. 3). The unpaired spin density data for both five-coordinate one-electron reduced **[1-Re]**^{0} and **[1-Mn]**^{0} complexes is similar to their counterparts with the Me_2OQN^- ligand, but an inspection of Mulliken charges indicates an increased electron density on each metal center in the latter as expected from the anionic nature of the Me_2OQN^- ligand (Fig. SI-16). The electrochemical redox potentials for both **[2-Re-MeCN]** and **[2-Mn-MeCN]** have been investigated by cyclic voltammetry and are presented below in Figure 4. For cyclic voltammetry plots directly comparing **[1-M-MeCN]**$^+$ and **[2-M-MeCN]** (M = Mn or Re) complexes, the reader is referred to the supporting information (Figs. SI-3 and SI-4).

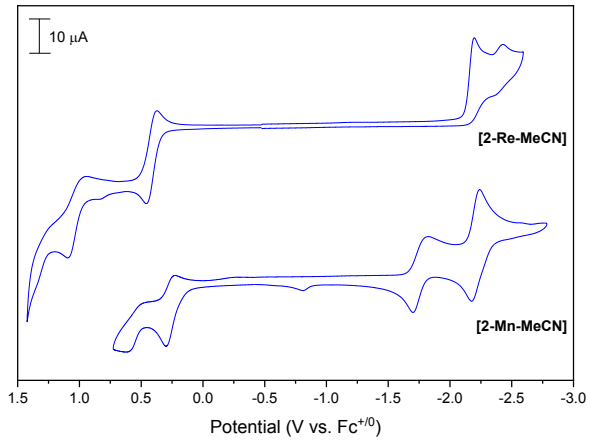

Figure 4. Cyclic voltammograms of **[2-Re-MeCN]** and **[2-Mn-MeCN]** recorded under 1 atm of argon with a 3 mm glassy carbon disc working electrode, and 1 mM analyte concentration in 0.1 M [Bu_4N][PF_6] acetonitrile supporting electrolyte with a scan rate of 0.10 V s^{-1}.

The voltammetry of Re bpy complexes is well established.[9] As shown in Fig. SI-3 for **[1-Re-MeCN]**$^+$, a quasi-reversible one-electron oxidation event occurs at +1.49 V vs the ferricenium/ferrocene ($Fc^{+/0}$) pseudo-reference redox couple (all potentials are hereafter reported vs $Fc^{+/0}$). Due to the electron rich character of the Me_2OQN^- ligand in **[2-Re-MeCN]**, its first oxidation occurs at +0.40 V (Fig. 4), which is >1 V negative of the Re(II/I) couple in **[1-Re-MeCN]**$^+$. Negligible Re(II) character is present in **[2-Re-MeCN]**$^+$. Furthermore, this primarily ligand-based **[2-Re-MeCN]**$^{(+/0)}$ redox couple is reversible. It is only upon 2-electron oxidation at +1.00 V that the redox chemistry of **[2-Re-MeCN]**$^{(2+/+)}$ becomes quasi-reversible likely due to decreased Re $d(\pi)\rightarrow$CO(π^*) back-bonding and CO dissociation. The reductive chemistry of **[1-Re-MeCN]**$^+$ follows an electrochemical-electrochemical-chemical (*EEC*) mechanism, as follows. The bpy(π^*)-based LUMO of **[1-Re-MeCN]**$^+$ is electronically independent of the Re(I) center. However, it is still redox-active and displays a quasi-reversible one-electron reduction at –1.61 V, followed by the Re(I/0) couple at –1.78 V (Fig. SI-3). This second reduction is irreversible due to dissociation of the monodentate acetonitrile ligand, forming the five coordinate, two-electron reduced [Re^0($bpy^{\bullet-}$)($CO)_3$]$^-$ species, which has previously been established as the active catalyst for

CO_2 reduction.[14] Upon switching the bpy ligand in cationic **[1-Re-MeCN]**$^+$ to the anionic Me_2OQN^- ligand in the neutral **[2-Re-MeCN]** complex, two irreversible one-electron reduction events are observed at –2.23 and –2.46 V (Fig. 4). As will be described below via computational and spectroelectrochemical EPR analysis, these are both assigned to the $Me_2OQN^{(-/\bullet-)}$ redox couple according to an *ECE* mechanism. The first $Me_2OQN^{(-/\bullet-)}$-based reduction forms the anionic $[Re^I(Me_2OQN^{\bullet-})(CO)_3(CH_3CN)]^-$ intermediate, which gives rise to dissociation of the monodentate acetonitrile ligand, facilitating a thermal migration of the added electron density onto the Re center to form the anionic five coordinate $[Re^0(Me_2OQN)(CO)_3]^-$ intermediate, allowing for a second ligand-based reduction to generate $[Re^0(Me_2OQN^{\bullet-})(CO)_3]^{2-}$.

The reductive chemistry of **[1-Mn-MeCN]**$^+$ is now also well established and follows an *ECE* mechanism.[1] The first reduction of **[1-Mn-MeCN]**$^+$ at –1.48 V is bpy(π*) based (Fig. SI-4). This is followed by rapid dissociation of the monodentate CH_3CN ligand, forming the five-coordinate neutral $[Mn^0(bpy)(CO)_3]$ metalloradical, which rapidly dimerizes to form $[Mn^0(bpy)(CO)_3]_2$. Subsequent reduction of this Mn^0–Mn^0 dimer is observed at –1.83 V, giving rise to the two-electron reduced five coordinate $[Mn^0(bpy^{\bullet-})(CO)_3]^-$ active catalyst. Notably, oxidation of the Mn^0–Mn^0 dimer is observed at –0.61 V upon the reverse scan in cyclic voltammetry. The Mn-Me_2OQN based complex, **[2-Mn-MeCN]** exhibits analogous electrochemical behavior to the **[2-Re-MeCN]** system albeit with slightly more positive potentials, occurring at –1.66 V and –2.21 V, forming the $[Mn^0(Me_2OQN)(CO)_3]^-$ and $[Mn^0(Me_2OQN^{\bullet-})(CO)_3]^{2-}$ five-coordinate mono- and di-anions, respectively (Scheme 2, Figure 4). In addition, a weak anodic peak is evident at –0.81 V. This is tentatively assigned to oxidation of the monoanionic $[Mn(Me_2OQN)(CO)_3]_2^-$ dimer likely formed by displacement of the solvent ligand in **[2-Mn-MeCN]** by the $[Mn^0(Me_2OQN)(CO)_3]^-$ metalloradical via Mn^I–Mn^0 bond formation. This is discussed further below in the pulse-radiolysis TRIR section. A collection of all redox potentials is provided here in Table 1 for reference.

Scheme 2. The electrochemical-chemical-electrochemical (*ECE*) mechanism exhibited by [2-Mn-MeCN] and [2-Re-MeCN] upon sequential two-electron reduction

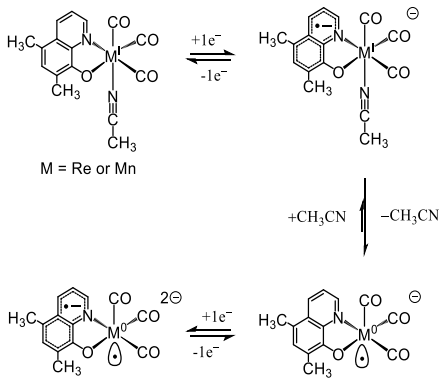

Table 1. Electrochemical data recorded in 0.1 M $[Bu_4N][PF_6]$ acetonitrile supporting electrolyte under 1 atm of argon at a glassy carbon working electrode with a scan rate of 0.10 V s^{-1}

E (V vs. $Fc^{+/0}$)					
[1-Re-MeCN]$^+$		+1.49[b]	–1.61[b]	–1.78[a]	–2.94[a]
[2-Re-MeCN]	+1.00[b]	+0.40[c]	–2.23[a]	–2.46[a]	
[1-Mn-MeCN]$^+$	+1.03[a]	–0.61[d]	–1.48[a]	–1.83[a]	–2.94[b]
[2-Mn-MeCN]	+0.62[a]	+0.27[c]	–0.81[d]	–1.66[b]	–2.21[c]

[a] irreversible, E_{pc} or E_{pa} tabulated [b] quasi-reversible [c] reversible [d] E_{pa} associated with dimer oxidation

Cyclic voltammetry under 1 atm of CO_2

Upon repeating cyclic voltammetry under 1 atm of CO_2 (0.28 M) in acetonitrile with 0.17 M H_2O present, catalytic current is observed to grow in for **[1-Re-MeCN]**$^+$ at its second reduction wave, consistent with the well-established two-electron reduced species $[Re^0(bpy^{\bullet-})(CO)_3]^-$ being the active catalyst. This five-coordinate anionic catalyst can react with CO_2 in the presence of a proton source, in this case H_2O, to generate the neutral $[Re(bpy)(CO)_3(CO_2H)]$ metallocarboxylic acid intermediate, which proceeds to evolve H_2O and CO upon further reduction. The full catalytic cycle for this reaction, and for the remaining catalysts in this study, is discussed in further detail below in the computational section; for the time being we will focus on the identity of each active catalyst generated in-situ. In contrast, and remarkably, **[2-Re-MeCN]** shows clear evidence for the onset of catalytic current upon the first one-electron reduction event when recorded under 1 atm of CO_2 (Fig. 5, $E_{cat/2} = –2.27$ V).

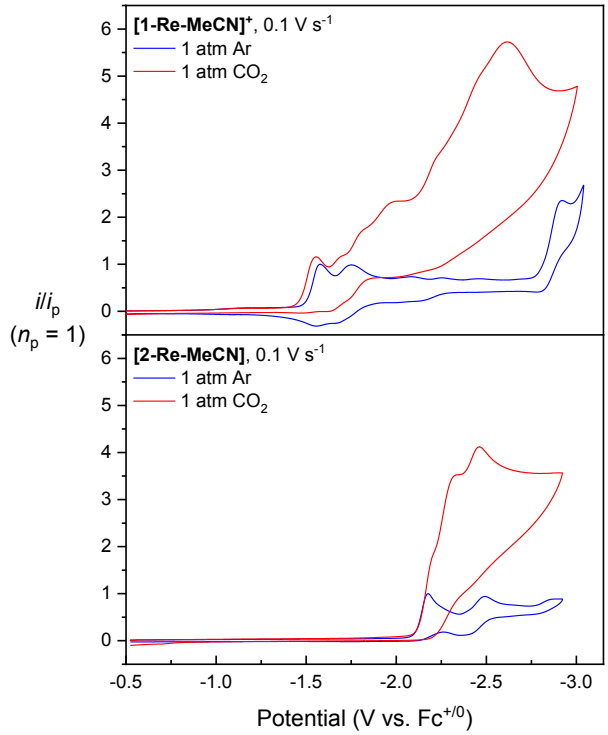

Figure 5. Cyclic voltammograms of **[1-Re-MeCN]**$^{+}$ (top) and **[2-Re-MeCN]** (bottom) recorded with 1 mM analyte concentration in 0.1 M [Bu$_4$N][PF$_6$] acetonitrile electrolyte with 0.17 M H$_2$O, under 1 atm of argon (blue) and 1 atm of CO$_2$ (red) at a 3 mm glassy carbon disc working electrode with a scan rate of 0.10 V s^{-1}. Both sets of voltammograms are normalized with respect to the non-catalytic Faradaic current, i_p, observed at the peak of the first reduction wave under argon (n_p is the number of electrons involved in the non-catalytic Faradaic current response).

The magnitude of the catalytic current response exhibits first-order kinetic behavior with respect to the concentration of **[2-Re-MeCN]** (Fig. SI-5), providing support for our hypothesis that the Me$_2$OQN$^{(\bullet/-)}$ redox couple is working in synergy with the Re(I/0) couple to initiate formation of the key [Re^{I}(Me$_2$OQN$^{\bullet}$)(CO)$_3$(CO$_2$H)] intermediate along the CO$_2$ reduction catalytic cycle. Although the coulombic impact of the negatively charged Me$_2$OQN^{-} ligand requires a more negative potential to form the one-electron reduced derivative relative to **[1-Re-MeCN]**$^{+}$, the **[2-Re-MeCN]** pre-catalyst exhibits a sharper growth of catalytic current likely due to its inherently greater nucleophilicity. It is also noteworthy that a second peak is exhibited at –2.46 V under catalytic conditions likely due to a parallel catalytic cycle stemming from the two-electron reduced **[2-Re]**$^{2-}$ active catalyst.

Recent evidence has shown that, while Mn-based catalysts can also bind CO$_2$, due to the lesser nucleophilicity of Mn vs Re they typically require a larger overpotential than their Re counterparts to drive catalytic CO formation at a similar rate to Re.[1, 15] This is due to the relatively lower energy of first-row vs. third-row valence *d*-orbitals. The electrocatalytic properties of **[1-Mn-MeCN]**$^{+}$ have already been discussed at great length elsewhere.[1] In the context of this study, it is important to appreciate that following two-electron reduction to form the five-coordinate [Mn^{0}(bpy$^{\bullet-}$)(CO)$_3$]$^{-}$ active catalyst, a large overpotential is observed due to the required reduction of the [Mn(bpy)(CO)$_3$(CO$_2$H)] intermediate in order to provide enough driving force for the rate-determining, proton-mediated C–OH bond cleavage step. The need for this additional reduction step to promote rate-determining C-OH bond cleavage is characteristic of most Mn-based catalysts and is commonly referred to as the *reduction-first* catalytic pathway.[1] In contrast to **[1-Mn-MeCN]**$^{+}$, pre-catalyst **[2-Mn-MeCN]** exhibits onset for catalytic current directly upon formation of the two-electron reduced [Mn(Me$_2$OQN)(CO)$_3$]$^{2-}$ intermediate (Fig. 6), thus avoiding any excessive overpotential beyond in-situ generation of the active catalyst ($E_{cat/2}$ = –1.95 V). This is consistent with pre-catalyst **[2-Mn-MeCN]** undergoing the proton-mediated C–OH bond cleavage step immediately upon two-electron reduction. In fact there is a significant anodic shift of the catalytic wave ($E_{cat/2}$ = –1.95 V) relative to the second-reduction wave observed under inert conditions (E = –2.21 V), might be due to the binding of CO$_2$ (Fig. 6).

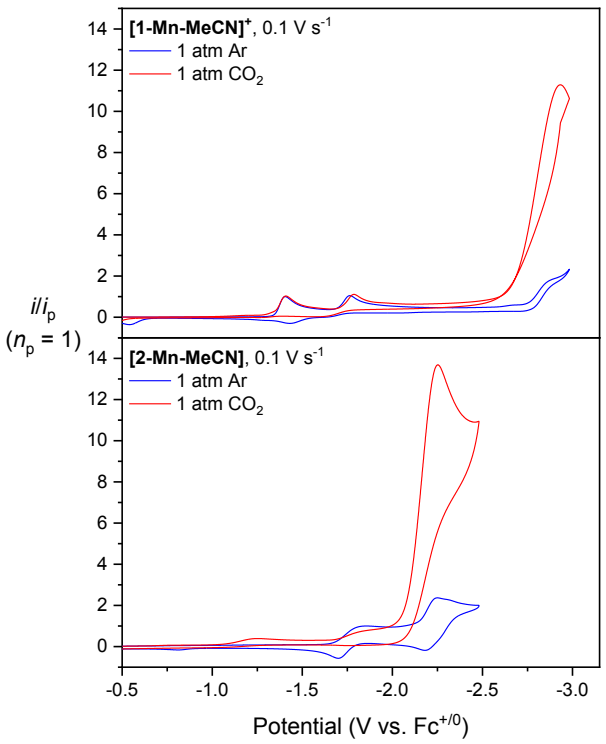

Figure 6. Cyclic voltammograms of **[1-Mn-MeCN]**$^{+}$ (top) and **[2-Mn-MeCN]** (bottom) recorded with 1 mM analyte concentration in 0.1 M [Bu$_4$N][PF$_6$] acetonitrile + 0.17 M H$_2$O electrolyte, under 1 atm of argon (blue) and 1 atm of CO$_2$ (red) at a 3 mm glassy carbon disc working electrode with a scan rate of 0.10 V s^{-1}. Both sets of voltammograms are normalized with respect to the non-catalytic Faradaic current, i_p, observed at the peak of the first reduction wave under argon (n_p is the number of electrons involved in the non-catalytic Faradaic current response).

To summarize, in comparison to **[1-Re-MeCN]**$^{+}$ and **[1-Mn-MeCN]**$^{+}$, the Me$_2$OQN^{-} based pre-catalysts exhibit onset of catalytic current with the input of one less equivalent of electrons to access the rate-determining C–OH bond cleavage step. Furthermore, both **[2-Re-MeCN]** and **[2-Mn-MeCN]** exhibit first-order kinetics with respect to both catalyst and CO$_2$ concentration (Figs. SI-5 through SI-8). At least for the **[2-Re-MeCN]** pre-catalyst, this behavior is attributed to the formal Me$_2$OQN$^{(\bullet/-)}$ redox couple which contributes in tandem with the Re(I/0) redox couple to CO$_2$/H^{+} activation (see computational section below for more details). In contrast to **[2-Re-MeCN]**, the **[2-Mn-MeCN]** pre-catalyst still requires two-electron reduction to access the metallocarboxylic acid intermediate. Direct onset of catalytic current from the two-electron reduced pentacoordinate species **[2-Mn]**$^{2-}$ is likely the consequence of a beneficial coulombic effect allowing for direct protonation to access the protonation mediated rate-determining C–OH bond cleavage step. In contrast, the bpy-based pre-catalyst **[1-Mn-MeCN]**$^{+}$ is converted to the pentacoordinate **[1-Mn]**$^{-}$ active catalyst in-situ, but upon CO$_2$/H^{+} binding to form the **[Mn-CO$_2$H]** intermediate a further reduction event, and inherent overpotential, is required to form the anionic **[Mn-CO$_2$H]**$^{-}$ intermediate to access the rate-determining step via the so-called *reduction-first* catalytic pathway.

A comparison of scan-rate dependent catalytic (i_{cat}) and non-catalytic (i_p) current ratio, i.e. scan-rate dependence of i_{cat}/i_p, allows for the identification of steady-state kinetic conditions and estimation of the maximum obtainable turnover frequency (TOF_{max}) for a well-behaved catalyst according to eq. 1,

$$TOF = 0.1992\left(\frac{F\upsilon}{RT}\right)\left(\frac{n_p^3}{n_{cat}^2}\right)\left(\frac{i_{cat}}{i_p}\right)^2 \qquad (1)$$

where F is the Faraday constant (96,485 s A mol^{-1}), υ is the scan rate (V s^{-1}), R is the universal gas constant (8.3145 V A s K^{-1} mol^{-1}), T is the temperature (K), n_p is the number of electrons involved in the non-catalytic Faradaic current response (responsible for i_p), and n_{cat} is the number of electrons required for catalysis (2 electrons for the reduction of CO_2 to CO). A plot of TOF vs scan rate for both **[2-Re-MeCN]** and **[2-Mn-MeCN]** is presented in Figure 7.

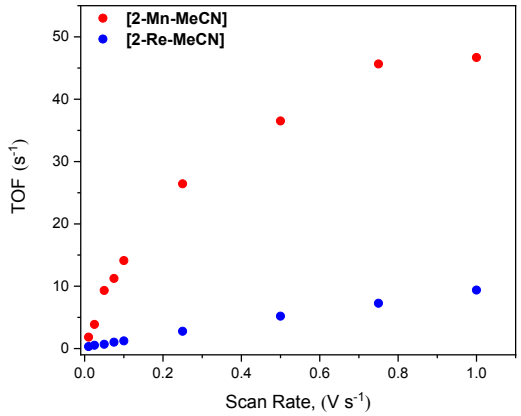

Figure 7. Scan-rate dependence of the turnover frequency (TOF) observed for **[2-Re-MeCN]** and **[2-Mn-MeCN]** recorded in 0.1 M $[Bu_4N][PF_6]$ acetonitrile electrolyte with 0.17 M H_2O under 1 atm of CO_2. Steady-state kinetic conditions for **[2-Mn-MeCN]** are identified above a threshold scan rate of $\upsilon \geq 0.75$ V s^{-1} by a plateau of the TOF response.

Steady-state conditions are established for **[2-Mn-MeCN]** at $\upsilon \geq 0.75$ V s^{-1}, resulting in an estimate of a TOF_{max} value of 45.4 ± 8.4 s^{-1}. Unfortunately, steady-state conditions could not be verified for pre-catalysts **[1-Re-MeCN]**$^+$, **[1-Mn-MeCN]**$^+$ and **[2-Re-MeCN]**, as upon increasing the scan-rate their TOFs continued with a linear progression with no signs of a plateau current (Fig. SI-9). While this may be construed (incorrectly) as a consequence of rapid catalyst turnover, the inherently low i_{cat}/i_p ratios suggest this is a consequence of catalyst inhibition by an unknown side-reaction and not rate-limiting CO_2 substrate consumption. Attempts to estimate TOF_{max} using Saveant's foot-of-the-wave analysis (FOWA) method were unsuccessful due to the weak catalytic currents observed and the limited linear portion of the sigmoidal current response.[35, 36] As such, the best-case alternative was to compare the i_{cat}/i_p ratios and non-optimized TOF values at a single scan rate of $\upsilon = 0.10$ V s^{-1} (Table 2).

Table 2. Summary of catalytic results for all complexes investigated. Results obtained from CV data recorded for 1 mM [catalyst] under 1 atm of CO_2 at 0.10 V s^{-1}

	$E_{cat/2}$ [a]	i_{cat}/i_p	TOF (s^{-1}) [b]
[1-Re-MeCN]$^+$	–2.25	3.6	2.6
[2-Re-MeCN]	–2.27	2.5	1.2
[1-Mn-MeCN]$^+$	–2.86	10.7	22.2
[2-Mn-MeCN]	–1.95	8.5	14.1

[a]Potentials reported as V vs. $Fc^{+/0}$. [b]TOF values estimated from the ratio i_{cat}/i_p determined at $\upsilon = 1.0$ V s^{-1} using eq. 1.

Notably, the **[1-Mn-MeCN]**$^+$ pre-catalyst exhibits the greatest TOF at 0.10 V s^{-1} in the presence of 1 atm of CO_2 and 0.17 M H_2O of 22.2 s^{-1}. This comes at the cost of the most negative $E_{cat/2}$ of –2.86 V. The **[2-Mn-MeCN]** catalyst exhibits a more favorable $E_{cat/2}$ of –1.95 V albeit with a slightly lower TOF of 14.1 s^{-1} under identical (non-steady state) experimental conditions. Both **[1-Re-MeCN]**$^+$ and **[2-Re-MeCN]** pre-catalysts exhibit smaller TOFs at just 2.6 s^{-1} and 1.2 s^{-1}, respectively.

Controlled potential electrolysis

To confirm the product selectivity of pre-catalysts **[1-Re-MeCN]**$^+$, **[2-Re-MeCN]**, **[1-Mn-MeCN]**$^+$ and **[2-Mn-MeCN]**, controlled potential electrolysis (CPE) experiments with quantitative in-situ gas chromatography analysis were run for CO and H_2 quantification followed by a single solution phase analysis of the electrolyte solution for formate quantification post-catalysis, using ion-exchange chromatography. In CPE experiments, each catalyst was reduced at a single potential bias identified by cyclic voltammetry (typically at $E_{cat/2}$) under 1 atm of CO_2 with 0.17 M H_2O. All four catalysts exhibit selective formation of CO, albeit with varying efficiencies, with negligible observation of H_2 and/or formate. Pre-catalyst **[1-Re-MeCN]**$^+$ exhibits a moderate Faradaic efficiency of 52% for CO. The Mn-based bpy analogue, **[1-Mn-MeCN]**$^+$ exhibits similar behavior with 62% Faradaic efficiency for CO and just a 2% Faradaic efficiency for H_2. The Me_2OQN^- based pre-catalyst, **[2-Re-MeCN]** presents a similarly moderate Faradaic efficiency for CO production relative to **[1-Re-MeCN]**$^+$, of 51%, with negligible H_2 at just 3%. However, pre-catalyst **[2-Mn-MeCN]**, exhibits almost quantitative CO evolution, with a Faradaic efficiency of 88%.

Table 2. Summary of Faradaic efficiencies achieved for each catalyst studied following 3 hours of controlled potential electrolysis

	CO (%) [a]	H_2 (%) [a]	HCO_2H (%) [b]
[1-Re-MeCN]$^+$	52	0	0
[2-Re-MeCN]	51	3	0
[1-Mn-MeCN]$^+$	62	2	0
[2-Mn-MeCN]	88	5	0

[a]Determined by GC chromatography, [b]Determined by ion-exchange chromatography

Attempts to account for missing Faradaic yield was unsuccessful. However, similar CPE experiments repeated in the presence of a larger excess of Brønsted acid, for example, 2.78 M (5%) H_2O, allowed for quantitative assignment of the Faradaic yield,

albeit with a much reduced selectivity for CO_2 reduction and increased H_2 yield. These data are summarized in Table SI-1.

Electron Paramagnetic Resonance Spectroscopy

Electron paramagnetic resonance (EPR) is a valuable, structurally sensitive technique to gain insight into the mechanistic steps for electrocatalysis pertaining to paramagnetic redox intermediates of transition metal catalysts. Furthermore, both naturally occurring isotopes of rhenium, ^{185}Re (37.1% abundance) and ^{187}Re (62.9% abundance), as well as the sole ^{55}Mn isotope (100% abundance), each possess a nuclear spin angular momentum of $I = 5/2$ giving rise to distinct hyperfine spectral features. EPR spectroscopy has already been employed in select studies to identify the nature of radical intermediates in the reduction of CO_2 using $[M(\alpha\text{-diimine})(CO)_3L]^n$, M = Mn or Re, based pre-catalysts. For example, Kubiak and coworkers recently used EPR to confirm the ligand-based radical in a $[Re(^{Mes}DAB^{Me\bullet-})]$ catalyst.[29] Kaim and coworkers have also used EPR extensively to study reduced states for a series of $[Re(bpy)(CO)_3L]^n$ pre-catalysts.[31] A comparable EPR response is here observed for **[1-Re-MeCN]**$^+$ following one-electron reduction (Fig. SI-10) where computation predicts the spin density to be predominantly based in a bpy(π^*) orbital (Fig. SI-16). In contrast to **[1-Re-MeCN]**$^+$, the Re center in **[2-Re-MeCN]** demonstrates notably different behavior after one-electron reduction (Fig. 8).

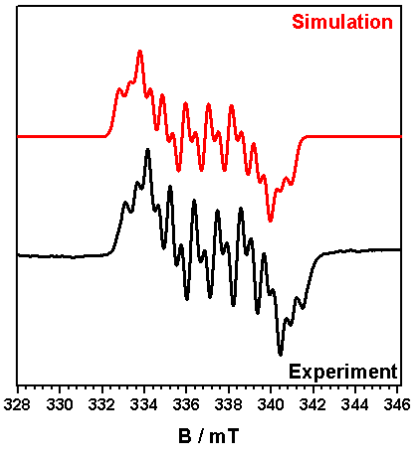

Figure 8. Experimental (X-band, 9.5 GHz, $g = 2.004$) and simulated EPR spectroelectrochemical data for **[2-Re-MeCN]** recorded at 77 K in 0.1 M $[Bu_4N][PF_6]$ acetonitrile electrolyte following one-electron reduction.

Clear evidence for an equilibrium mixture of two species is observed, consistent with the theoretical prediction for reversible dissociation of the acetonitrile solvent for the one-electron reduced species, i.e. **[2-Re-MeCN]**$^-$ ⇌ **[2-Re]**$^-$ + MeCN, to generate the pentacoordinate $[Re^0(Me_2OQN)(CO)_3]^-$ metalloradical complex with the Re center responsible for 22% of the spin character (Fig. 3). This result is highly significant as it provides clear experimental evidence of the latter metalloradical species which is believed to be the active catalyst for CO_2 reduction.

A broad EPR signal is observed upon one-electron reduction of **[1-Mn-MeCN]**$^+$, which is solely attributed to the hexacoordinate $[Mn^I(bpy^{\bullet-})(CO)_3(CH_3CN)]^0$ radical anion possessing a predominantly ligand-based radical (ρ_{Mn} = 0.00, Fig. SI-16). Again, hyperfine splitting is observed as a sextet consistent with coupling to the adjacent Mn^0 ($I = 5/2$) center (Fig. SI-11). It should be emphasized here that one-electron reduction of **[1-Mn-MeCN]**$^+$ leads to rapid formation of the EPR silent $[Mn(bpy)(CO)_3]_2$ dimer. However, EPR is a very sensitive technique and is capable of characterizing even trace quantities of $[Mn(bpy^{\bullet-})(CO)_3(CH_3CN)]^0$.

In contrast, the strong sextet EPR signal exhibited upon one-electron reduction of **[2-Mn-MeCN]** (Fig. 9) provides strong evidence for the pure Mn(0) based pentacoordinate metalloradical species $[Mn^0(Me_2OQN)(CO)_3]^-$. The lack of additional hyperfine splitting here suggests that there is limited interaction of the unpaired electron with surrounding nuclei on the ligand, concluding that the radical is entirely based on the Mn center. This observation is also consistent with computational studies, which predict a spin-density of ρ_{Mn} = 1.36 for $[Mn^0(Me_2OQN)(CO)_3]^-$ (Fig. 3).

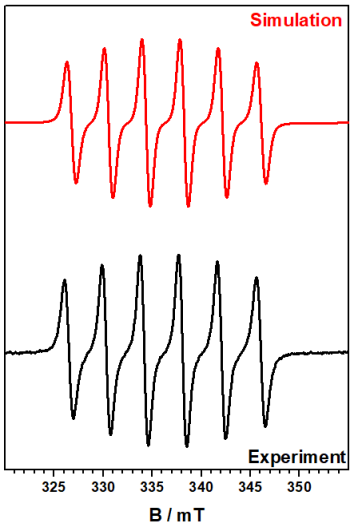

Figure 9. Experimental (X-band, 9.5 GHz) and simulated EPR spectroelectrochemical data for **[2-Mn-MeCN]** recorded at 77 K in 0.1 M $[Bu_4N][PF_6]$ acetonitrile electrolyte following one-electron reduction ($g = 2.007$).

Pulse Radiolysis Time-Resolved Infrared Spectroscopy

In pulse radiolysis (PR), a high-energy electron pulse from an accelerator is used to excite a sample.[37] This rapidly generates a homogeneous mixture of reducing and oxidizing radicals derived from the solvent, which include the strongly reducing solvated electron (e_s^-). Typically, an additive is used to scavenge undesired radicals and/or to convert the primary radicals into one type of radical species, thus creating either oxidizing or reducing conditions.[37] For the experiments discussed here in CH_3CN, formate ion ($OC(O)H^-$) was added to the solution as a radical scavenger. The H-atom transfer processes that it under-

goes with the solvent radicals rapidly generate the strongly reducing carbon dioxide radical anion ($CO_2^{\bullet-}$),[38] which, in addition to e_s^-, acts as a reductant towards the dissolved metal complex.

Combining PR with nanosecond time-resolved infrared (TRIR) detection has provided a powerful tool for mechanistic studies of electrocatalysts since specific redox intermediates can be rapidly prepared and identified, and their reactivity subsequently monitored.[1, 39, 40] Indeed, PR-TRIR has the time resolution to allow the detection of short-lived intermediates that cannot be observed by infrared spectroelectrochemistry (IR-SEC). For example, previous PR-TRIR studies of the mononuclear $[Mn(dtbpy)(CO)_3(OC(O)H)]$ pre-catalyst in CH_3CN[39] allowed the observation of formate dissociation from the one-electron reduced $[Mn(dtbpy^{\bullet-})(CO)_3(OC(O)H)]^-$ transient (τ = 77 ns) with concomitant production of the neutral five-coordinate $[Mn^0(dtbpy)(CO)_3]$ radical, and dimerization of this radical to form the Mn–Mn bound $[Mn^0(dtbpy)(CO)_3]_2$ dimer. In contrast, PR-TRIR has also been used to demonstrate the absence of dimerization upon one-electron reduction of pre-catalysts that generate the bulky $[Mn^0(mes_2bpy)(CO)_3]$ and $\{Mn^0([(MeO)_2Ph]_2bpy)(CO)_3\}$ intermediates.[3] In these cases, the two-electron reduced species was observed to grow-in on the microsecond timescale, consistent with disproportionation of the one-electron reduced intermediate,[3] as previously implied by CV and IR-SEC experiments.[41, 42]

Upon preparation of solutions of **[2-Re-MeCN]** and **[2-Mn-MeCN]** for PR-TRIR experiments in CH_3CN in the presence of 50 mM $[Bu_4N][OC(O)H]$ as a solvent radical scavenger, the large excess of formate ions quantitatively generated the **[2-Re-OC(O)H]**$^-$ and **[2-Mn-OC(O)H]**$^-$ anions in-situ, due to the strong coordinating nature of formate compared with CH_3CN. However, these complexes still contain the Me_2OQN^- ligand and metal centers in the M(I) oxidation state, thus allowing interpretation of any catalytic intermediates upon formate dissociation, since Mn-formate complexes have previously been shown to rapidly eject the formate ligand upon one-electron reduction.[3, 39] **[2-Re-OC(O)H]**$^-$ exhibits three ν(CO) bands at 2003, 1885 and 1866 cm^{-1} in CH_3CN (Fig. 10, bottom). Upon one-electron reduction by PR, these peaks are bleached, giving immediate rise to two new ν(CO) stretching modes at 1975 and 1843(br) cm^{-1} (Fig. 10, top). By comparison with computed IR spectra of all reasonable intermediates at the M06 level of theory (Fig. SI-12), we assign these bands to the one-electron reduced, coordinatively unsaturated $[Re^0(Me_2OQN)(CO)_3]^-$ anion produced upon formate dissociation, which is expected[39] to be extremely rapid (nanosecond timescale). Within 2 μs, another band grows-in at 1997 cm^{-1}. Again by comparison with computed IR spectra (Fig. SI-12), this is attributed to the A(1)′ ν(CO) stretch of the hexacoordinate $[Re(Me_2OQN^{\bullet-})(CO)_3(CH_3CN)]^-$ solvated anion, with both its A(2)′ and A″ ν(CO) stretches obscured by the strong doublet bleach of the formate starting material. The latter is evident by a positive valley in the bleach signal at 1875 cm^{-1} (Fig. 10).

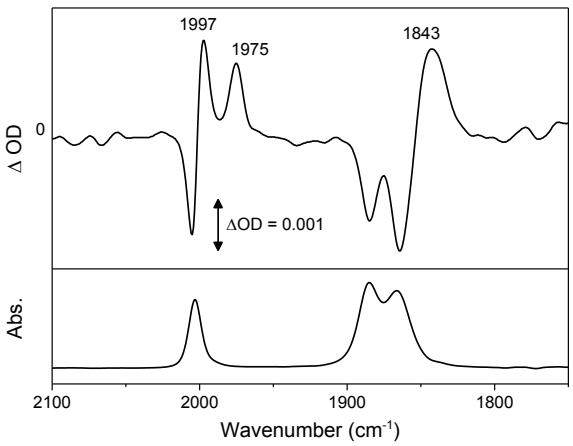

Figure 10. IR spectrum of a 1.5 mM solution of **[2-Re-OC(O)H]**$^-$ in CH_3CN containing 50 mM $[^nBu_4N][OC(O)H]$ (bottom) and the TRIR spectrum recorded 2 μs after pulse radiolysis of this argon-purged solution (top).

The abovementioned PR-TRIR observations are consistent with the EPR and computational analysis of **[2-Re-MeCN]** with respect to equilibria between the pentacoordinate $[Re^0(Me_2OQN)(CO)_3]^-$ metalloradical and the hexacoordinate $[Re(Me_2OQN^{\bullet-})(CO)_3(CH_3CN)]^-$ solvated anion. These species were found to decay at different rates on the microsecond timescale, with the latter being more unstable. This is not surprising, since it was previously shown that formate ion only scavenges 60 ± 20% of the radiolytic solvent radicals in CH_3CN,[38] and thus the remaining radicals are likely to react with these two species at different rates due to their distinct radical characters. Since the actual decay pathways are unknown in the PR experiment, we will not discuss them further here.

[2-Mn-OC(O)H]$^-$ exhibits three ν(CO) stretches at 2013, 1909 and 1887 cm^{-1} in CH_3CN (Fig. 11, bottom). All three are instantly bleached upon one-electron reduction by PR, giving immediate rise to a pair of sharp and broad ν(CO) bands at 1928 and 1810 cm^{-1}, respectively (Fig. 11, top). The latter peaks are consistent with IR-SEC experiments (Fig. SI-13) upon one-electron reduction of **[2-Mn-MeCN]**, and are assigned to the five-coordinate $[Mn^0(Me_2OQN)(CO)_3]^-$ metalloradical by comparison with the computed IR spectrum of this species (Fig. SI-14). Sole observation of the one-electron reduced $[Mn^0(Me_2OQN)(CO)_3]^-$ metalloradical is also consistent with EPR and computational analysis of **[2-Mn-MeCN]**, and this species is found to decay slowly on the few hundred microseconds timescale, similar to the Re analog. Interestingly, there is also tentative evidence for a weak band at 2032 cm^{-1} in the PR-TRIR spectrum (Fig. 11), which may correspond to a possible $[Mn(Me_2OQN)(CO)_3]_2^-$ dimer, also observed by infrared spectroelectrochemistry (IR-SEC) at 1866(br), 1877 and 2032 cm^{-1} (Figs. SI-13 & SI-15). Such dimer formation, albeit minor, may also be responsible for the weak oxidation wave observed at –0.81 V by cyclic voltammetry (Fig. 4, Table 1).

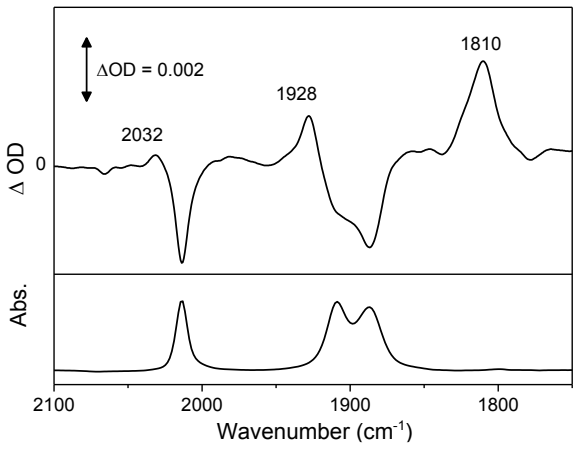

Figure 11. IR spectrum of a 1.5 mM solution of **[2-Mn-OC(O)H]**$^-$ in CH_3CN containing 50 mM [^{n}Bu$_4$N][OC(O)H] (bottom) and the TRIR spectrum recorded 15 μs after pulse radiolysis of this argon-purged solution (top).

Computational analysis

We performed density functional theory calculations at the M06-L and M06 level of theories coupled with the SMD continuum solvation model for acetonitrile (see computational methods for further details) to investigate the mechanism for proton-coupled electrocatalytic CO_2 reduction catalyzed by both **[2-Re-MeCN]** and **[2-Mn-MeCN]**, including the electronic structures of catalytic intermediates, to produce CO and H_2O. The proposed catalytic cycle is presented in Scheme 3 including the computed standard reduction potentials ($E°$), free energy changes (ΔG) and activation free energies ($\Delta G^‡$). Plots of molecular orbitals and spin densities, are provided in the supporting information alongside the optimized transition-state structures for C–OH bond cleavage (Fig. SI-17). Here, the computed energetics at the M06 level of theory are presented with comparable data at the M06-L level of theory also available in supporting information. The proposed mechanism starts with a one-electron reduction step with concomitant dissociation of the acetonitrile ligand leading to the formation of **[2-M]**$^-$ for both **[2-Mn-MeCN]** and **[2-Re-MeCN]** with computed $E°$ of –1.68 V and –2.25 V vs $Fc^{+/0}$, respectively, in quite good agreement with cyclic voltammetry experiments. The computed ΔGs indicate that acetonitrile dissociation is irreversible for **[2-Mn]**$^-$ (ΔG = –18.7 kcal/mol) whereas it's possible to have an equilibrium in the case of **[2-Re]**$^-$ (ΔG = –1.4 kcal/mol). This is consistent with spectroelectrochemical EPR and PR-TRIR experiments. Acetonitrile dissociation upon one-electron reduction is also favorable for **[1-Mn-MeCN]**$^+$ (ΔG = –6.6 kcal/mol) but is unfavorable for **[1-Re-MeCN]**$^+$ (ΔG = 4.1 kcal/mol), also consistent with our experimental observations. As discussed above, in the resulting pentacoordinate species the spin is mostly localized on the metal center for **[2-Mn]**$^-$ (ρ_{Mn} = 1.36) whereas it is delocalized across both the ligand and the metal center for **[2-Re]**$^-$ (ρ_{Re} = 0.22).

Following the first reduction, CO_2 binding to **[2-Re]**$^-$ (ΔG = 12.6 kcal/mol) is possible whereas we could not locate a CO_2 bound adduct for the **[2-Mn]**$^-$ species, which is in line with the observed increase in catalytic current only for **[2-Re-MeCN]** at its first reduction potential (Fig. 5). Following CO_2 binding and protonation (ΔG = –11.2 kcal/mol at pH 0) the neutral **[2-Re-CO$_2$H]** metallocarboxylic intermediate of formula [Re^I(Me$_2$OQN$^•$)(CO)$_3$(CO$_2$H)] is generated. Formation of the latter species is key to the unique electrocatalytic behavior exhibited by the **[2-Re-MeCN]** pre-catalyst. Consistent with a redox contribution from the Me$_2$OQN$^-$ ligand towards CO_2 reduction is how radical character is calculated to be delocalized predominantly across the phenolate-side of the Me$_2$OQN$^•$ ring (ρ_{Me2OQN} = 0.88) with just a weak contribution from the formal Re^{II} (ρ_{Re} = 0.05) oxidation state. This ligand-based oxidation is really triggered by protonation of the **[2-Re-CO$_2$]**$^-$ adduct (ρ_{Re} = 0.27; ρ_{CO2} = 0.59) which still possesses the Me$_2$OQN$^-$ ligand in its native anionic state (Fig. 12).

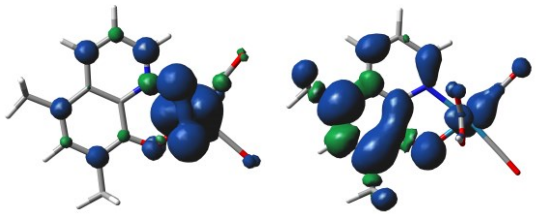

[2-Re-CO$_2$]$^-$ (ρ_{Re} = 0.27; ρ_{CO2} = 0.59)

[2-Re-CO$_2$H] (ρ_{Me2OQN} = 0.88; ρ_{Re} = 0.05)

Figure 12. Spin density plots (isofactor = 0.001) computed at the M06 level of theory illustrating the significant contribution of the one-electron oxidized Me$_2$OQN$^•$ ligand to the **[2-M-CO$_2$H]** catalytic intermediate in contrast to its **[2-Re-CO$_2$]**$^-$ precursor.

A facile reduction ($E°$ = –0.23 V) is then predicted to regenerate the native Me$_2$OQN$^-$ ligand oxidation state to result in the formation of **[2-Re-CO$_2$H]**$^-$. The computed energetics indicate that subsequent protonation resulting in C–OH bond cleavage is rate-limiting ($\Delta G^‡$ = 29.3 kcal/mol) while the following one-electron reduction step to form **[2-Re-CO]**$^-$ is quite facile. In the case of the **[2-Mn-MeCN]** pre-catalyst, further reduction of the one-electron reduced intermediate, **[2-Mn]**$^-$, to **[2-Mn]**$^{2-}$ is required for CO_2 binding (ΔG = 0.7 kcal/mol), which upon protonation (ΔG = –41.8 kcal/mol) leads to formation of **[2-Mn-CO$_2$H]**$^-$. Next, C–OH bond cleavage assisted by water as the Brønsted acid is proposed to occur with a computed activation free energy, $\Delta G^‡$ = 27.8 kcal/mol for **[2-Mn-CO$_2$H]**$^-$. Further one-electron reduction of the C–OH bond cleavage products, **[Re-CO]** and **[Mn-CO]**, followed by facile CO evolution, regenerates the active [M]$^-$ intermediate completing the catalytic cycle. For the **[1-Mn-MeCN]**$^+$ and **[1-Re-MeCN]**$^+$ pre-catalysts, C–OH bond cleavage exclusively proceeds via the *reduction–first pathway* in the present conditions, whereas this path is not accessible with **[2-Mn-MeCN]** and **[2-Re-MeCN]** due to high overpotential requirements for the reduction of [M-CO$_2$H]$^-$ to [M-CO$_2$H]$^{2-}$ ($E°$ = –2.75 V and –2.58 V for **[2-Mn-MeCN]** and **[2-Re-MeCN]**, respectively). We have previously reported on the activation of this thermodynamically favorable *protonation-first* pathway utilizing Lewis base moieties in the second-coordination sphere of a Mn-bpy based pre-catalyst.[3] However, to the best of our knowledge, this is the first example of a Mn pre-catalyst providing access to the *protonation-first* pathway via inner coordination sphere effects. This behavior is not surprising when the electron-rich character of the Me$_2$OQN$^-$ ligand is considered relative to bpy. Essentially, formation of the **[2-**

Mn-CO_2H]$^-$ intermediate precludes an additional reduction step as it already carries a negative charge upon its formation, facilitating direct access to the *protonation-first* pathway and avoiding an excessive overpotential. As a result, in comparison to **[1-Mn-MeCN]$^+$** and **[1-Re-MeCN]$^+$** pre-catalysts, the Me_2OQN^--based pre-catalysts exhibit onset of catalytic current with the input of one less equivalent of electrons to access the rate-determining C–OH bond cleavage step. Moreover, the computed $\Delta G^{\ddagger}$s predict an order of magnitude faster CO evolution by **[2-Mn-MeCN]** compared to **[2-Re-MeCN]**, in line with the experimentally observed TOFs.

Scheme 3. Proposed catalytic cycles for pre-catalysts **[2-Re-MeCN]** and **[2-Mn-MeCN]** including computed $E°$ (vs $Fc^{+/0}$), ΔG (kcal/mol) and $\Delta G^{\ddagger}$ (kcal/mol) at the M06 level of theory

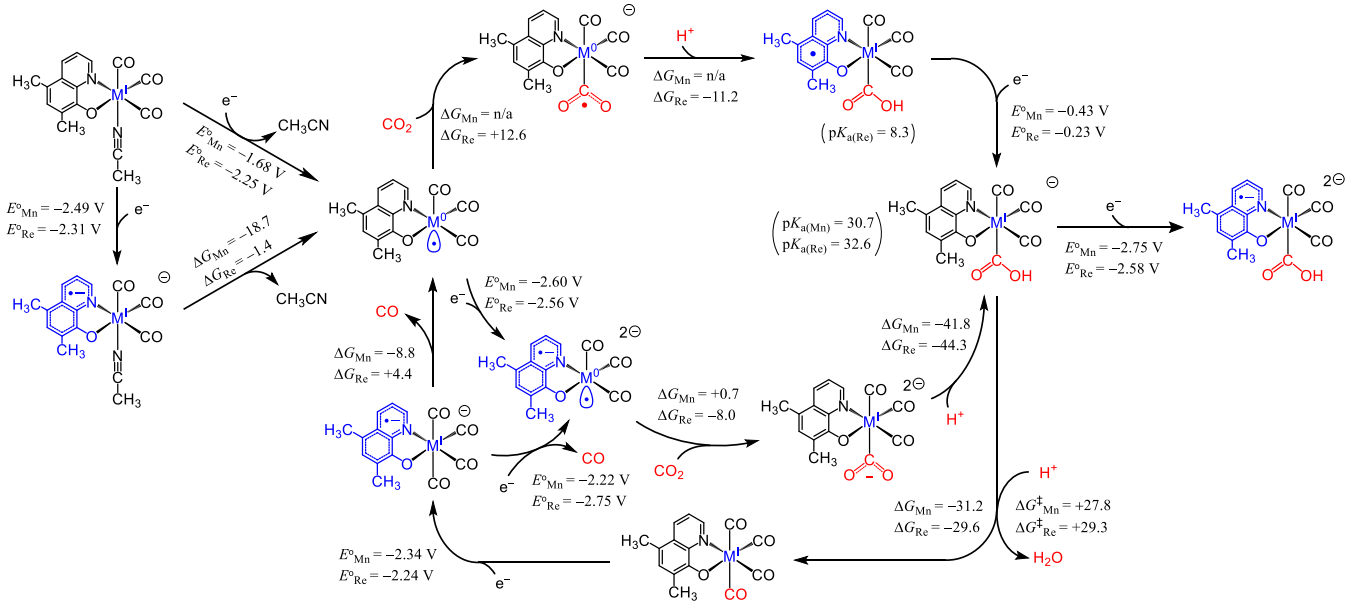

CONCLUSION

The electronic properties for both Mn and Re complexes of the general formula $[M(Me_2OQN)(CO)_3(CH_3CN)]$ have been presented and distinguished from their reference bpy-based analogues. The non-innocent Me_2OQN^- ligand imparts unique electrochemical properties to the **[2-Mn-MeCN]** and **[2-Re-MeCN]** pre-catalysts which make them particularly suited to electrocatalytic applications. In particular, under 1 atm of CO_2 and in the presence of H_2O as a Brønsted acid, electrocatalytic CO_2 reduction is demonstrated for both **[2-Mn-MeCN]** and **[2-Re-MeCN]** pre-catalysts. Onset of catalytic current for both **[2-Mn-MeCN]** and **[2-Re-MeCN]** is initiated with the input of one less equivalent of electrons relative to their bpy-based reference complexes, $[M(bpy)(CO)_3(CH_3CN)]^+$ (M = Mn or Re). Utilizing spectroelectrochemical EPR, FTIR and computational analysis, in addition to the powerful technique of PR-TRIR spectroscopy, it was possible to narrow down the one-electron and two-electron reduced species relevant for the exhibition of CO_2 reduction activity. In particular, for **[2-Re-MeCN]**, the formal $Me_2OQN^{(\bullet/-)}$ redox couple contributes towards each catalytic cycle in tandem with the formal $Re^{I/0}$ redox couples by facilitating in-situ generation of the active catalyst and driving the rate-determining C–OH bond cleavage step upon just one-electron reduction of the pre-catalyst. In contrast, **[2-Mn-MeCN]** requires the input of a second electron to activate the catalyst. However, the coulombic influence of the Me_2OQN^- ligand precludes the need for an additional overpotential associated with the *reduction-first* pathway, facilitating a *protonation-first* CO_2 reduction pathway for both **[2-Mn-MeCN]** and **[2-Re-MeCN]** pre-catalysts.

EXPERIMENTAL SECTION

Materials and Methods

The following chemicals were purchased from Sigma Aldrich; bromopentacarbonylmanganese(I) (98%), silver trifluoromethanesulfonate (>99%), tetrabutylammonium hexafluorophosphate (>99%), potassium carbonate (>99%), 2,2,2-trifluoroethanol (>99%), tetrahydrofuran (anhydrous, 99.9%), hexane (ACS reagent grade, 99%), acetonitrile (ACS reagent grade, >99.5%). Tetrabutylammonium hexafluorophosphate was recrystallized thrice from ethanol and dried under vacuum prior to electrolyte preparation. The water content in ACS reagent grade acetonitrile was confirmed by Karl-Fisher titration to be 0.17 M (0.3%). Steady-state FTIR spectra were recorded on a Thermo Nicolet 670 FTIR spectrophotometer in spectrophotometric grade acetonitrile. NMR spectra were recorded on an Agilent spectrometer operated at 399.80 MHz for ^1H nuclei. CD_3CN was used as received from Sigma Aldrich and its resid-

ual ^{1}H solvent signal (δ = 1.94 ppm)[43] used as an internal reference for reporting the chemical shift. Voltammetry and bulk electrolysis were carried out on a CH Instruments 620E potentiostat. A custom three electrode cell was used for both voltammetry and bulk electrolysis experiments allowing airtight introduction of working, counter and reference electrodes as well as septa for gas purging. For cyclic voltammetry, glassy carbon (3 mm diameter) and Pt wire were used as working and counter electrodes, respectively, with 0.1 M $[Bu_4N][PF_6]$ in spectrophotometric grade acetonitrile as the supporting electrolyte. A non-aqueous reference electrode was used to minimize ohmic potential drop at the solvent interface. This consisted of a Ag wire in 0.10 M $[Bu_4N][PF_6]$ acetonitrile supporting electrolyte isolated by a Vycor frit and was calibrated in-situ using the ferricenium/ferrocene redox couple as a pseudo reference. Redox potentials (E) were determined from cyclic voltammetry as (E_{pa} + E_{pc})/2, where E_{pa} and E_{pc} are the anodic and cathodic peak potentials respectively. Where E could not be calculated due to irreversible behavior, E_{pc} or E_{pa} are reported accordingly. For CO_2 concentration dependent studies, gas cylinders were ordered from Airgas containing pre-mixed ratios of Ar:CO_2 (100:0, 80:20, 60:40, 50:50, 40:60, 20:80, 0:100).

Controlled potential electrolysis & product quantification

For controlled potential bulk electrolysis experiments, a vitreous carbon (Structure Probe, Inc.) working electrode soldered to a copper wire was used. A Pt gauze counter electrode was used, isolated from the main compartment by a fine porosity Vycor tube+frit to minimize resistance. Gas chromatography data were recorded on a custom Shimadzu GC-2014 instrument where a Ni "methanizer" catalyst was used to convert CO to CH_4 prior to quantification of CH_4 by the thermal conductivity detector. H_2 was simultaneously monitored by a flame ionization detector during the same injection. The GC was precalibrated for CO and H_2 quantification by mimicking bulk electrolysis conditions (i.e. 5 mL supporting electrolyte in the same cell, with electrodes, under 1 atm CO_2). Standard curves for H_2 and CO were generated using this cell where known volumes of the analyte gas (H_2 or CO) were injected and the solution stirred for 30 min to allow equilibration of the analyte between the electrolyte and headspace prior to GC injection. Formate analysis following bulk electrolysis was completed using a Dionex Aquion instrument using a Dionex IonPac AS22 (4 x 250 mm) anion column and Dionex AERS 500 Carbonate (4 mm) electrolytically regenerated suppressor. Samples were prepared for analysis by diluting an aliquot of the bulk electrolysis solution by a factor of ten in deionized water. Filtration to remove insoluble $[Bu_4N][PF_6]$ electrolyte was required using a PVDF 0.22 μm syringe filter. The diluent and mobile phase consisted of a sodium carbonate:bicarbonate (4.5:1.4) solution run at 0.70 mL/min at room temperature. The formate peak was observed at 6.23 min and integrated to quantify the concentration of formic acid produced in reference to a standard calibration curve.

Synthesis

[Mn(Me$_2$OQN)(CO)$_3$(THF)] To a microwave vial, ~3 mL of dry THF was left to purge gently with argon. To this vial, the ligand, 5,7-dimethyl-8-hydroxyquinoline (63 mg, 0.36 mmol) was added with a three-fold excess of K_2CO_3 (150 mg, 1.09 mmol). This reaction solution was left to stir for approximately 1 minute under argon. The manganese starting material, bromopentacarbonyl manganese(I) (100 mg, 0.36 mmol), was then added. The reaction vial was sealed quickly and irradiated at 60°C for approximately 1 hour. Upon cooling, the reaction mixture, a bright orange-red solution, was filtered through a small plug of alumina, removing the insoluble base. Recrystallization with hexanes yielded analytically pure product as a shiny yellow solid in 28% yield. FTIR (CH_3CN) ν(CO): 2032, 1938, 1915 cm^{-1}. ^{1}H-NMR (CD_3CN) δ: 2.34 (3H, s), 2.51 (3H, s), 7.20 (1H, s), 7.46 (1H, dd, J_1 = 4 Hz, J_2 = 8 Hz), 8.37 (1H, dd, J_1 = 2 Hz, J_2 = 4 Hz), 8.98 (1H, dd, J_1 = 2 Hz, J_2 = 4 Hz). Anal. Calcd. for $C_{18}H_{18}MnNO_5$: C, 56.41; H, 4.73; N, 3.65. Found: C, 56.82; H, 4.89; N, 3.48.

Electron paramagnetic resonance (EPR) spectroscopy

EPR spectra at X-band frequency (ca. 9.5 GHz) were obtained with a Magnettech MS-5000 benchtop EPR spectrometer equipped with a rectangular TE 102 cavity. The measurements were carried out in synthetic quartz glass tubes. For EPR spectroelectrochemistry a three-electrode setup was employed using two Teflon-coated platinum wires (0.005" bare, 0.008" coated) as working (or a Teflon-coated gold wire (0.003" bare, 0.0055" coated) as working electrode) and counter electrode and a Teflon-coated silver wire (0.005" bare, 0.007" coated) as a pseudoreference electrode. All spectra were recorded at 77 K in 0.1 M $[Bu_4N][PF_6]$ acetonitrile following controlled potential electrolysis. Spectral simulations were performed with EasySpin 5.1.4 and MatLab R2012a.

Pulse Radiolysis Step-Scan FTIR Experiments

Pulse radiolysis experiments were conducted at the 2 MeV Van de Graaff (VdG) electron accelerator located in the Chemistry Division at Brookhaven National Laboratory. A commercial step-scan FTIR spectrometer (Bruker, Vertex 80v) equipped with an external fast risetime HgCdTe IR detector was placed on an air-stabilized optical bench close to the VdG's electron beam line exit window, with the electron beam passing directly through a homemade, air-tight IR flow cell (0.7 mm pathlength) equipped with 0.5 mm thick CaF_2 windows. A 25 mL CH_3CN solution containing 1.5 mM of the Mn complex and 0.025 M tetrabutylammonium formate (synthesized according to a reported procedure[39]) was prepared inside a glovebox and placed into a sealed reservoir vessel. The vessel was then inserted into a gas-tight recirculating flow system containing a magnetically-coupled gear pump (Micropump). The tubing was evacuated and refilled with argon several times before saturating the solution with 2 atm argon and flowing. The VdG can produce electron pulses of increasing dose by increasing the electron pulse-width up to a maximum of 5 μs. In these experiments, we used 500 ns electron pulses at a repetition rate of 5 Hz. Since our experiments were not quantitative, we did not measure the absorbed dose. The time-resolved step-scan FTIR measurements were performed in a manner similar to those previously reported[44] for laser flash photolysis, except in this case a digital delay generator (Stanford Research Systems, DG535) was used to trigger the electron pulses in synchronization with the data collection. A preamplifier built into the IR detector was used to amplify the detector signal prior to digitization. In a typical experiment, data were collected at 6 cm^{-1} spectral resolution with an optical band pass filter that resulted in 255 interferogram

mirror positions. 16 averages were acquired at each mirror position, leading to a total of 4080 electron pulses impinging on the flowing sample. FTIR spectra recorded after the experiment showed very little overall sample decomposition (< 5 %).

Computational Methods

Density functional theory. All geometries were fully optimized at the M06-L[45] and M06 levels of density functional theory[46-48] with the SMD continuum solvation model[49] for acetonitrile as solvent using the Stuttgart [8s7p6d2f | 6s5p3d1f] ECP10MDF contracted pseudopotential basis set[50] on Mn, the Stuttgart [8s7p6d2f | 6s5p3d2f] ECP60MWB contracted pseudopotential basis set[51] on Re and the 6-31G(d) basis set on all other atoms.[52] Non-analytical integrals were evaluated using the integral=grid=ultrafine option as implemented in the Gaussian 16 software package.[53] The nature of all stationary points was verified by analytic computation of vibrational frequencies, which were also used for the computation of zero-point vibrational energies, molecular partition functions, and for determining the reactants and products associated with each transition-state structure (by following the normal modes associated with imaginary frequencies). Partition functions were used in the computation of 298 K thermal contributions to the free energy employing the usual ideal-gas, rigid-rotator, harmonic oscillator approximation.[54] Free-energy contributions were added to single-point, SMD-solvated M06-L and M06 electronic energies computed at the optimized geometries obtained with the initial basis with the SDD basis set on Mn and Re, and the larger 6-311+G(2df,p) basis set on all other atoms to arrive at final, composite free energies.

Solvation and standard reduction potentials. As mentioned above, solvation effects for acetonitrile were accounted for by using the SMD continuum solvation model. A 1 M standard state was used for all species in solution (except for acetonitrile as solvent for which the standard state was assigned as 19.14 M). Thus, the free energy in solution is computed as the 1 atm gas-phase free energy, plus an adjustment for the 1 atm to 1 M standard-state concentration change of *RT* ln (24.5), or 1.9 kcal/mol, plus the 1 M to 1 M transfer (solvation) free energy computed from the SMD model. Standard reduction potentials were calculated for various possible redox couples to assess the energetic accessibility of different intermediates at various oxidation states. For a redox reaction of the form

$$O_{(aq)} + n\,e^-_{(g)} \rightarrow R_{(aq)} \qquad (2)$$

where *O* and *R* denote the oxidized and reduced states of the redox couple, respectively, and *n* is the number of electrons involved in redox reaction, the reduction potential $E^{o}_{O|R}$ relative to SCE was computed as

$$E^{o}_{O|R} = -\frac{\Delta G^{o}_{O|R}}{nF} - \Delta E^{o}_{ref} \qquad (3)$$

where $\Delta G^{o}_{O|R}$ is the free energy change associated with eq. 2 (using Boltzmann statistics for the electron) and ΔE^{o}_{ref} is taken as 0.141 V,[55] which is required for the conversion of calculated $E^{o}_{O|R}$ versus normal hydrogen electrode (NHE) in aqueous solution (E_{NHE}=-4.281 V)[56] to $E^{o}_{O|R}$ versus the saturated calomel electrode (SCE) in acetonitrile (E_{SCE} = -4.422 V).[57] We obtained reduction potentials referenced to the ferricenium/ferrocene couple by using a shift of -0.384 V from $E^{o}_{O|R}$ vs SCE.

ASSOCIATED CONTENT

Supporting Information

NMR and FTIR spectra of **[2-Mn-MeCN]**, cyclic voltammetry, catalyst and CO_2 concentration dependence, TOF overlay plot, spectroelectrochemical EPR and FTIR, computational FTIR, spin-density plots and transition state geometries.

The Supporting Information is available free of charge on the ACS Publications website.

AUTHOR INFORMATION

Corresponding Authors

E-mail addresses:

jonathan.rochford@umb.edu (J. Rochford)

dcgrills@bnl.gov (D.C. Grills)

mzertem@bnl.gov (M.Z. Ertem)

ACKNOWLEDGMENT

J.R. thanks the National Science Foundation for support under grant number CHE-1301132. The work at BNL (D.C.G. and M.Z.E.), including use of the Van de Graaff facility of the BNL Accelerator Center for Energy Research (ACER), was supported by the U.S. Department of Energy (DOE), Office of Basic Energy Sciences, Division of Chemical Sciences, Geosciences & Biosciences, under contract No. DE-SC0012704. K.T.N. is grateful to the DOE for an Office of Science Graduate Student Research (SCGSR) award. Some of this research used resources of the Center for Functional Nanomaterials (CFN) for the fabrication of optics for PR-TRIR experiments and computational modeling studies. The CFN is a U.S. DOE Office of Science Facility at Brookhaven National Laboratory, operating under contract No. DE-SC0012704.

REFERENCES

1. Grills, D. C.; Ertem, M. Z.; McKinnon, M.; Ngo, K. T.; Rochford, J., *Coord. Chem. Rev.* **2018,** *374*, 173-217.

2. Francke, R.; Schille, B.; Roemelt, M., *Chem. Rev.* **2018,** *118*, 4631-4701.

3. Ngo, K. T.; McKinnon, M.; Mahanti, B.; Narayanan, R.; Grills, D. C.; Ertem, M. Z.; Rochford, J., *J. Am. Chem. Soc.* **2017,** *139*, 2604-2618.
4. Franco, F.; Pinto, M. F.; Royo, B.; Lloret-Fillol, J., *Angew. Chem. Int. Ed.* **2018,** *57*, 4603-4606.
5. Walsh, J. J.; Neri, G.; Smith, C. L.; Cowan, A. J., *Chem. Commun.* **2014,** *50*, 12698-12701.
6. Reuillard, B.; Ly, K. H.; Rosser, T. E.; Kuehnel, M. F.; Zebger, I.; Reisner, E., *J. Am. Chem. Soc.* **2017,** *139*, 14425-14435.
7. Hawecker, J.; Lehn, J. M.; Ziessel, R., *J. Chem. Soc., Chem. Commun.* **1984**, 328-330.
8. Hawecker, J.; Lehn, J. M.; Ziessel, R., *Helv. Chim. Acta* **1986,** *69*, 1990-2012.
9. Sullivan, B. P.; Bolinger, C. M.; Conrad, D.; Vining, W. J.; Meyer, T. J., *J. Chem. Soc., Chem. Commun.* **1985**, 1414-1415.
10. Bourrez, M.; Molton, F.; Chardon-Noblat, S.; Deronzier, A., *Angew. Chem. Int. Ed.* **2011,** *50*, 9903-9906.
11. Franco, F.; Cometto, C.; Vallana, F. F.; Sordello, F.; Priola, E.; Minero, C.; Nervi, C.; Gobetto, R., *Chem. Commun.* **2014,** *50*, 14670-14673.
12. Rao, G. K.; Pell, W.; Korobkov, I.; Richeson, D., *Chem. Commun.* **2016,** *52*, 8010-8013.
13. Franco, F.; Cometto, C.; Nencini, L.; Barolo, C.; Sordello, F.; Minero, C.; Fiedler, J.; Robert, M.; Gobetto, R.; Nervi, C., *Chem. Eur. J.* **2017,** *23*, 4782-4793.
14. Riplinger, C.; Sampson, M. D.; Ritzmann, A. M.; Kubiak, C. P.; Carter, E. A., *J. Am. Chem. Soc.* **2014,** *136*, 16285-16298.
15. Riplinger, C.; Carter, E. A., *ACS Catal.* **2015,** *5*, 900-908.
16. Agarwal, J.; Shaw, T. W.; Stanton III, C. J.; Majetich, G. F.; Bocarsly, A. B.; Schaefer III, H. F., *Angew. Chem. Int. Ed.* **2014,** *53*, 5152-5155.
17. Stanton III, C. J.; Vandezande, J. E.; Majetich, G. F.; Schaefer III, H. F.; Agarwal, J., *Inorg. Chem.* **2016,** *55*, 9509-9512.
18. Spall, S. J. P.; Keane, T.; Tory, J.; Cooker, D. C.; Adams, H.; Fowler, H.; Meijer, A.; Hartl, F.; Weinstein, J. A., *Inorg. Chem.* **2016,** *55*, 12568-12582.
19. Matsuzaki, R.; Suzuki, S.; Yamaguchi, K.; Fukui, T.; Tanizawa, K., *Biochemistry* **1995,** *34*, 4524-4530.
20. Tabuchi, K.; Ertem, M. Z.; Sugimoto, H.; Kunishita, A.; Tano, T.; Fujieda, N.; Cramer, C. J.; Itoh, S., *Inorg. Chem.* **2011,** *50*, 1633-1647.
21. Vu, V. V.; Ngo, S. T., *Coord. Chem. Rev.* **2018,** *368*, 134-157.
22. Turner, N. J., *Chem. Rev.* **2011,** *111*, 4073-4087.
23. Jørgensen, C. K., *Coord. Chem. Rev.* **1966,** *1*, 164-178.
24. Kaim, W., *Inorg. Chem.* **2011,** *50*, 9752-9765.
25. Allgeier, A. M.; Mirkin, C. A., *Angew. Chem., Int. Ed.* **1998,** *37*, 895-908.
26. Chaudhuri, P.; Wieghardt, K., *Prog. Inorg. Chem.* **2001,** *50*, 151-216.
27. Muckerman, J. T.; Polyansky, D. E.; Wada, T.; Tanaka, K.; Fujita, E., *Inorg. Chem.* **2008,** *47*, 1787-1802.
28. Lyaskovskyy, V.; de Bruin, B., *ACS Catal.* **2012,** *2*, 270-279.
29. van der Meer, M.; Rechkemmer, Y.; Peremykin, I.; Hohloch, S.; van Slageren, J.; Sarkar, B., *Chem. Commun.* **2014,** *50*, 11104-11106.
30. Lacy, D. C.; McCrory, C. C. L.; Peters, J. C., *Inorg. Chem.* **2014,** *53*, 4980-4988.
31. Scheiring, T.; Klein, A.; Kaim, W., *J. Chem. Soc., Perkin Trans. 2* **1997**, 2569-2571.
32. Zhao, H. C.; Mello, B.; Fu, B.-L.; Chowdhury, H.; Szalda, D. J.; Tsai, M.-K.; Grills, D. C.; Rochford, J., *Organometallics* **2013,** *32*, 1832-1841.
33. Torralba-Peñalver, E.; Luo, Y.; Compain, J.-D.; Chardon-Noblat, S.; Fabre, B., *ACS Catal.* **2015,** *5*, 6138-6147.
34. Kaim, W., *Eur. J. Inorg. Chem.* **2012**, 343-348.
35. Costentin, C.; Drouet, S.; Robert, M.; Savéant, J.-M., *Science* **2012,** *338*, 90-94.
36. Costentin, C.; Passard, G.; Savéant, J.-M., *J. Am. Chem. Soc.* **2015,** *137*, 5461-5467.
37. Grills, D. C.; Polyansky, D. E.; Fujita, E., *ChemSusChem* **2017,** *10*, 4359-4373.
38. Grills, D. C.; Lymar, S. V., *Phys. Chem. Chem. Phys.* **2018,** *20*, 10011-10017.
39. Grills, D. C.; Farrington, J. A.; Layne, B. H.; Lymar, S. V.; Mello, B. A.; Preses, J. M.; Wishart, J. F., *J. Am. Chem. Soc.* **2014,** *136*, 5563-5566.
40. Grills, D. C.; Farrington, J. A.; Layne, B. H.; Preses, J. M.; Bernstein, H. J.; Wishart, J. F., *Rev. Sci. Instrum.* **2015,** *86*, 044102.
41. Sampson, M. D.; Nguyen, A. D.; Grice, K. A.; Moore, C. E.; Rheingold, A. L.; Kubiak, C. P., *J. Am. Chem. Soc.* **2014,** *136*, 5460-5471.
42. Sampson, M. D.; Kubiak, C. P., *J. Am. Chem. Soc.* **2016,** *138*, 1386-1393.
43. Fulmer, G. R.; Miller, A. J. M.; Sherden, N. H.; Gottlieb, H. E.; Nudelman, A.; Stoltz, B. M.; Bercaw, J. E.; Goldberg, K. I., *Organometallics* **2010,** *29*, 2176-2179.
44. Grills, D. C.; van Eldik, R.; Muckerman, J. T.; Fujita, E., *J. Am. Chem. Soc.* **2006,** *128*, 15728-15741.
45. Zhao, Y.; Truhlar, D. G., *J. Chem. Phys.* **2006,** *125*.
46. Zhao, Y.; Truhlar, D. G., *Theor. Chem. Acc.* **2008,** *120*, 215-241.
47. Zhao, Y.; Truhlar, D. G., *Acc. Chem. Res.* **2008,** *41*, 157-167.
48. Zhao, Y.; Truhlar, D. G., *Reviews in Mineralogy & Geochemistry* **2010,** *71*, 19-37.
49. Marenich, A. V.; Cramer, C. J.; Truhlar, D. G., *J. Phys. Chem. B* **2009,** *113*, 6378-6396.
50. Dolg, M.; Wedig, U.; Stoll, H.; Preuss, H., *Journal of Chemical Physics* **1987,** *86*, 866-872.
51. Andrae, D.; Häußermann, U.; Dolg, M.; Stoll, H.; Preuß, H., *Theor. Chim. Acta* **1990,** *77*, 123-141.
52. Hehre, W. J.; Radom, L.; Schleyer, P. v. R.; Pople, J. A., *Ab Initio Molecular Orbital Theory*. Wiley: New York, 1986.
53. Frisch, M. J.; Trucks, G. W.; Schlegel, H. B.; Scuseria, G. E.; Robb, M. A.; Cheeseman, J. R.; Scalmani, G.; Barone, V.; Petersson, G. A.; Nakatsuji, H.; Li, X.; Caricato, M.; Marenich, A. V.; Bloino, J.; Janesko, B. G.; Gomperts, R.; Mennucci, B.; Hratchian, H. P.; Ortiz, J. V.; Izmaylov, A. F.; Sonnenberg, J. L.; Williams; Ding, F.; Lipparini, F.; Egidi, F.; Goings, J.; Peng, B.; Petrone, A.; Henderson, T.; Ranasinghe, D.; Zakrzewski, V. G.; Gao, J.; Rega, N.; Zheng, G.; Liang, W.; Hada, M.; Ehara, M.; Toyota, K.; Fukuda, R.; Hasegawa, J.; Ishida, M.; Nakajima, T.; Honda, Y.; Kitao, O.; Nakai, H.; Vreven, T.; Throssell, K.; Montgomery Jr., J. A.; Peralta, J. E.; Ogliaro, F.; Bearpark, M. J.; Heyd, J. J.; Brothers, E. N.; Kudin, K. N.; Staroverov, V. N.; Keith, T. A.; Kobayashi, R.; Normand, J.; Raghavachari, K.; Rendell, A. P.; Burant, J. C.; Iyengar, S. S.; Tomasi, J.; Cossi, M.; Millam, J. M.; Klene, M.; Adamo, C.; Cammi, R.; Ochterski, J. W.; Martin, R. L.; Morokuma, K.; Farkas, O.; Foresman, J. B.; Fox, D. J. *Gaussian 16 Rev. A.03*, Wallingford, CT, 2016.
54. Cramer, C. J., *Essentials of Computational Chemistry: Theories and Models*. 2nd ed.; John Wiley & Sons: Chichester, 2004; p 385-427.
55. Keith, J. A.; Grice, K. A.; Kubiak, C. P.; Carter, E. A., *J. Am. Chem. Soc.* **2013,** *135*, 15823-15829.
56. Kelly, C. P.; Cramer, C. J.; Truhlar, D. G., *J Phys Chem B* **2006,** *110*, 16066-16081.
57. Isse, A. A.; Gennaro, A., *The Journal of Physical Chemistry B* **2010,** *114*, 7894-7899.